

# COMPUTERIZED X-RAY MICROTOMOGRAPHY OBSERVATIONS AND FLUID FLOW MEASUREMENTS OF THE EFFECT OF EFFECTIVE STRESS ON FRACTURED LOW PERMEABILITY POROUS MEDIA

Nathan J. Welch<sup>1</sup>, John P. Crawshaw<sup>1</sup>, and Edo S. Boek<sup>2</sup>

<sup>1</sup>Department of Chemical Engineering, Qatar Carbonates and Carbon Storage Research Centre, Imperial College London, South Kensington Campus, London SW7 2AZ, U.K.

<sup>2</sup>Department of Chemistry, Cambridge University

e-mail: [n.welch12@imperial.ac.uk](mailto:n.welch12@imperial.ac.uk)

*This paper was prepared for presentation at the International Symposium of the Society of Core Analysts held in St. John's Newfoundland and Labrador, Canada, 16-21 August, 2015*

## ABSTRACT

This work shows the observed changes in sample permeability and fracture geometry that occur within a fractured piece of low permeability shale with different effective stress gradients applied to the plug sample. These observations were made using an in-situ micro-CT fluid flow imaging apparatus with a carbon fibre Hassler-type core holder. Changes within the preferential fluid flow path under different stress regimes as well as physical changes to the fracture geometry are reported. Lattice-Boltzmann single phase permeability flow simulations were performed on the extracted flow paths and compared to experiment permeability measurements.

Experimental flow measurements showed significant changes in the permeability of the fractured system with varying stress states. Imaged fracture apertures were also used in simple parallel plate flow calculations, and compared to results from fluid flow simulations on segmented sample void space and experimental fluid flow measurements.

## INTRODUCTION

Ensuring the long-term safe geologic storage of carbon dioxide has become an important scientific and political issue for wide spread implementation of carbon dioxide sequestration operations. An intact and substantial seal formation above a storage reservoir is required for a significant portion of the initial sealing mechanisms believed to occur during carbon dioxide storage operations [1]. Shales and evaporites are common seal formation rock types found above numerous hydrocarbon reservoirs, as well as potential saline aquifer storage locations [2]. These seals are known for having very low permeabilities, however, some also have the tendency to be quite fissile, and the formation of fractures within these seals can have a significant detrimental effect on the sealing potential of a reservoir and amount to large areas of high permeability and low capillary pressures compared to the surrounding intact rock [3].

Work has continued to progress the rapid determination of these sealing parameters in the selection of suitable sequestration sites. A recent review of all available literature for capillary entry pressure measurements in an attempt to predict sealing characteristics of these seal formations shows the substantial lack of data available for interpretation [4]. Numerous experimental techniques have been developed for quickly determining these properties [5-9] with an overall comparison of each method presented by Boulin et al. [10]. Intact seal samples typically have nanometre sized pores as well as very low permeabilities, and fluid flow through fractures would largely dominate any observed fluid behaviour in the system. Fractures in these systems therefore allow for application of more traditional core analysis techniques [11] due to the rise in permeability and decrease in capillary pressure.

In this work, we were able to image the individual fractures found to be present in a fractured sample using our recently developed in-situ microtomography fluid flow apparatus. The purpose of this work is to attempt to relate observed changes in the sample fracture network geometry with varying system stress to changes in recorded fluid flow behaviour, and also to compare predicted fluid flow behaviour using simple equations for fluid flow between parallel plates and numerical fluid flow simulations, to experiment results.

## EXPERIMENT DESIGN

The fractured sample used in all of these observations was a cored plug sample taken from a large carboniferous shale quarry sample received from Todhills Long Lane Quarry in the UK. The sample was extracted via bulldozer from one of the working benches of the quarry and shrink-wrapped to try and prevent loss of natural pore fluid during shipping. The approximately 20 kg sample arrived after 2 days of shipping still in the original packaging material. Upon removal, the sample remained in one large roughly cube-shaped mass. The sample was then immediately wrapped in several layers of heavy black plastic and stored for later use.

High pressure mercury intrusion (Micromeritics AutoPore IV 9500, Cup and stem penetrometer) measurements were recorded on oven dried fragments collected from the larger mass shown in **Figure 1**. After drying, these fragments were further broken down into pieces no longer than 6 mm of any side length to fit into the mercury cup of the penetrometer. The majority of pores of the intact sample pore structure were <100nm in size, with a total porosity of 9.77%.

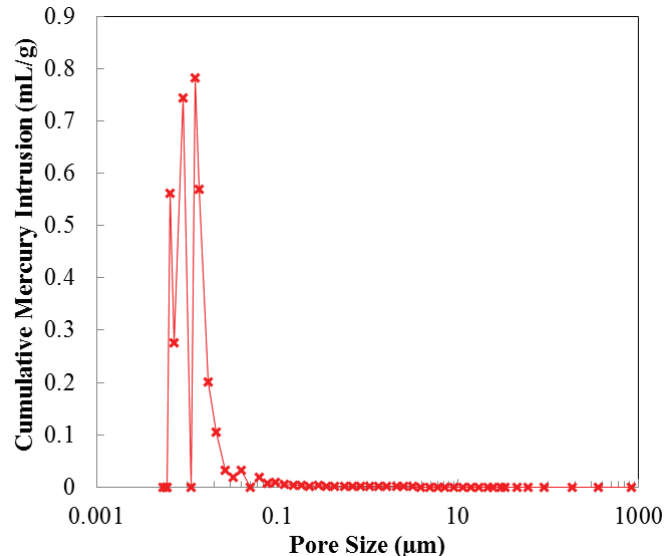


Figure 1: HPMI results for Long Lane Quarry shale

Large chunks of the original sample were broken away by hand with little force along natural cleavage planes of the sample for plug drilling. The sample's reactivity to water was immediately apparent on contact with tap water used for drilling. The sample began to fail along multiple parallel cleavage planes due to clay swelling and resulted in laminate sheets of about 1 cm in thickness. These smaller cleaved sheets still had a fairly high strength to them, and could not be broken by hand. In order to avoid the clay swelling, later plugs were instead drilled using compressed air to remove debris and cool the coring bit. The sample used in this study was drilled and then came into contact with untreated water resulting in the observed fracture network. This caused the sample to immediate begin to break apart due to swelling and it was then wrapped in PTFE tape to maintain the original configuration of fractured pieces.

Fluid flow measurements and x-ray microtomography observations were collected in our [12] micro-CT fluid flow apparatus designed for high resolution in-situ imaging of fluid flow behaviour in porous samples. Tomograms were collected with an Xradia XRM-500 computerized microtomography apparatus. A specially designed Hassler-type flow cell was used for this system designed by Airborne International. The flow cell has a maximum internal diameter of 19 mm, and can accommodate samples up to 212 mm in length. The flow cell is constructed of high strength carbon fibre for low x-ray absorbance, and sealed with stainless steel end caps. ISCO 260D syringe pumps were used to maintain all fluid pressures and record flow rates.

The fractured sample was then carefully removed from the PTFE tape and placed inside Viton tubing, while maintaining the original alignment of the fractured pieces. Current capabilities of the core holder system limits the system to only applying uniform confining pressure around the whole of the sample with no other axial stress provided.

## SINGLE PHASE PERMEABILITY OBSERVATIONS

After loading the sample into the fluid flow cell, water was used the annulus of the flow cell as the system's confining fluid. This was done to try to ensure the x-ray transmission of the dry scan was similar to that during fluid flow. A dry tomogram was recorded to show the zero-stress geometry of the system.

Avizo 9.0 produced by FEI [13] was used for initial tomogram visualization and manipulation. Orthogonal slices of the dry fractured sample can be seen in **Figure 2**. To avoid interference with image segmentation and later analyses, a region similar to the one represented with the white cornered rectangles in each plane was extracted from each 3D reconstruction recorded. This region of interest was selected to exclude end piece artefacts and the core sleeve, being the largest inscribed rectangular shape that could be fit within the sample. Registration and exact extraction of a similar region would have been more feasible if not for the rather high anisotropy of compressibility exhibited by the sample.

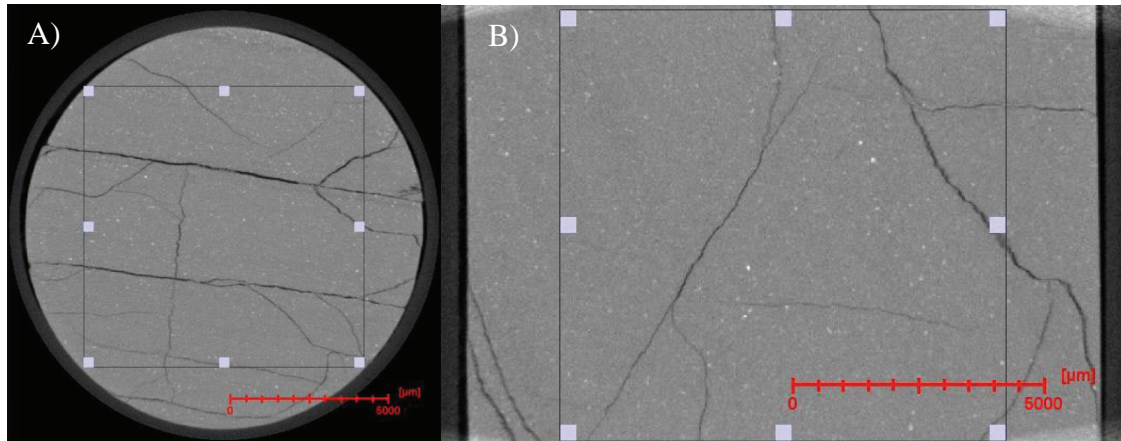


**Figure 2:** Orthogonal slices of the dry scan tomography highlighting the region of interest extracted avoiding x-ray artefacts in full 3D space. A) x-y and B) x-z orthogonal slice. All scale bars shown are a length of 5000  $\mu\text{m}$ .

Following the extraction of the region of interest, a noise-reducing, edge-preserving non-local means filter [14] was applied to the image data set to assist in image segmentation and analysis for the dry scan. Following dry scan imaging, 5wt% NaCl, 1wt% KCl brine was introduced to the sample and pressurized to an initial system pressure of 6 bar confining pressure, 5 bar upstream pressure, and 4 bar downstream pressure. This brine was selected to try and reduce further reactivity with changes in ion concentration within the shale matrix and pore fluid. No further fracturing was observed from the introduction of this wetting phase brine.

System stress was then varied, initially holding a constant pressure drop of 1 bar across the fractured sample, and incrementally increasing confining pressure of the system from 6 bar to 120 bar. After each change in system stress, a tomogram was recorded for the

system and permeability measurements recorded based on volume displacement in system pumps over the course of the scan. System scan times took on average 90-120 minutes for a  $13.2\text{-}13.7 \mu\text{m}$  cubic voxel side length tomogram.

A slice orthogonal to the flow direction from approximately the same location in the fractured system can be seen in **Figure 3** under no-stress, a low confining stress of 5 bar, and a high confining stress of 120 bar. The plane parallel to the major fractures has a much lower resistance to stress than those opposing the major fractures. This change in overall sample geometry also caused issues with direct visual comparison as the overall geometry of the system had changed between each change in system stress.

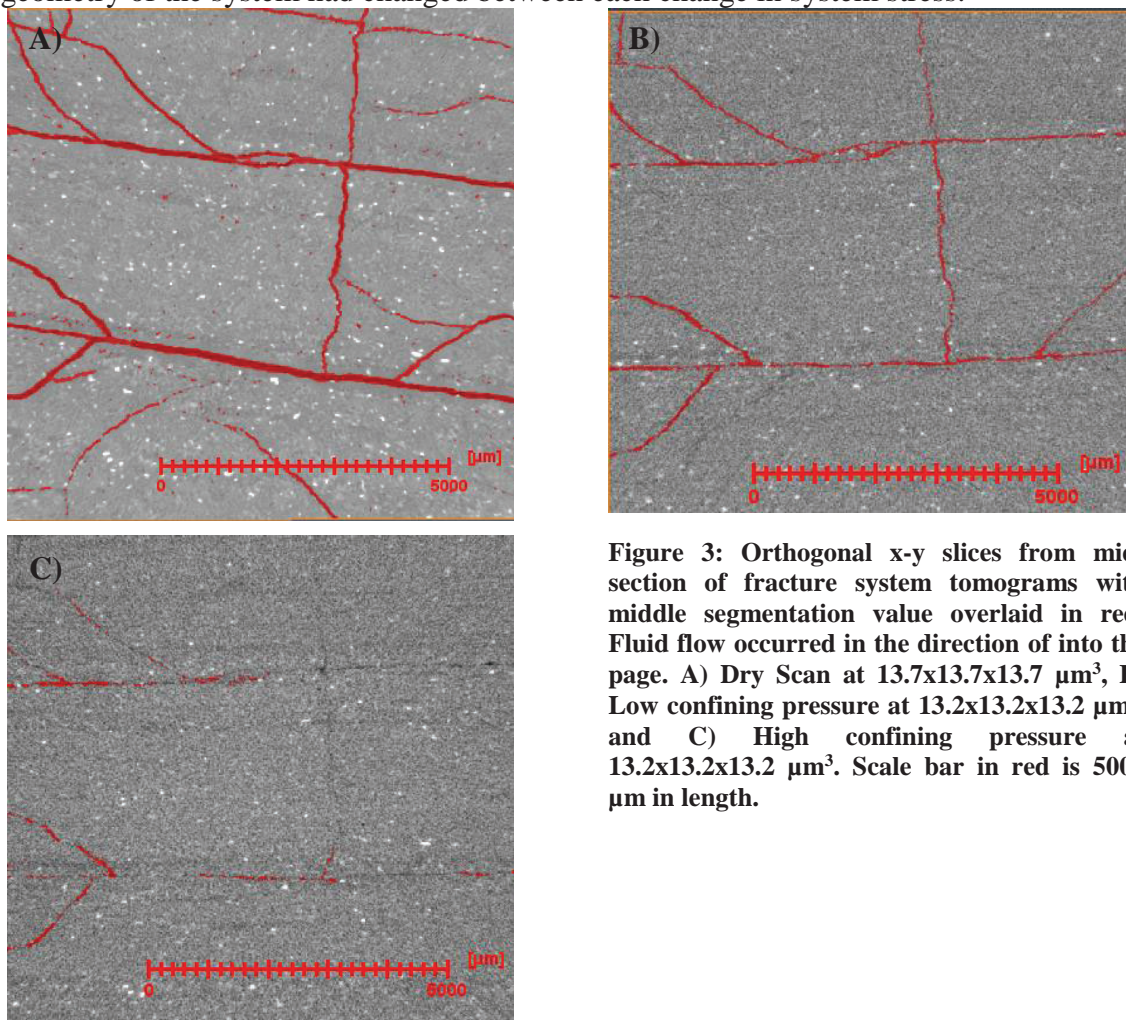


**Figure 3:** Orthogonal x-y slices from mid-section of fracture system tomograms with middle segmentation value overlaid in red. Fluid flow occurred in the direction of into the page. A) Dry Scan at  $13.7 \times 13.7 \times 13.7 \mu\text{m}^3$ , B) Low confining pressure at  $13.2 \times 13.2 \times 13.2 \mu\text{m}^3$ , and C) High confining pressure at  $13.2 \times 13.2 \times 13.2 \mu\text{m}^3$ . Scale bar in red is 5000  $\mu\text{m}$  in length.

Sample permeabilities were also recorded with changes in system stress with a varying pressure drop across the core. Finally, system permeabilities and tomograms were recorded for decreasing effective stress, or rising pore pressure. The permeability results for each different system stress can be seen in **Figure 4**. Initially confining fluid pressure was increased in logarithmic intervals from 6 to 120 bar. Then, only the upstream pressure was increased from 5 to 119 bar, with the maximum pressure selected to remain

just below the confining pressure of the system. Finally the downstream pressure was increased in similar intervals until a final pressure of 118 bar was reached.

The effective pressure of the system is defined in this work as the confining pressure minus the average of the inlet and outlet pore pressures. Error bars are reported as discrepancies found between upstream and downstream measurements, with minimal contribution to error with the in terms of the volume resolution of the pumps. One set of error bars on the highest stress data point for the rising confining pressure data series was omitted due to non-realistic flows found in the downstream pump. This non-realistic flow behaviour may have been due to either compression of gases trapped in the pore space or thermal variations within experimental environment.

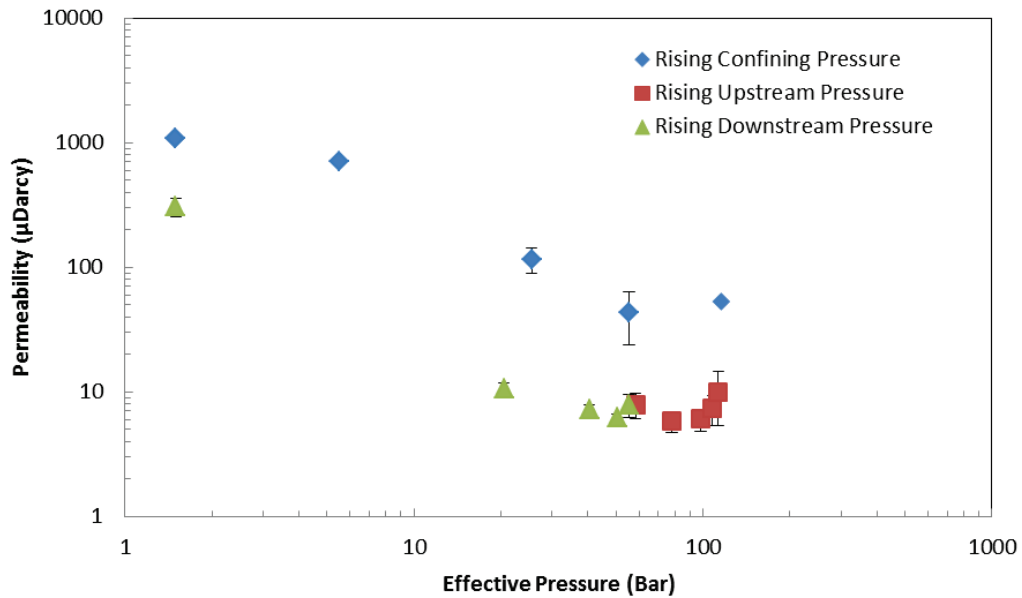


**Figure 4:** Changes in permeability of the fractured system due to changes in system stress.

The initial changes in permeability with increased confining pressure are expected as the overall aperture of the observed fractures was seen to decrease as the effective pressure of the system increased. During increasing upstream pressure, and overall differential pressure, permeability was seen to initially decrease with increasing pressure drop across the sample. This decrease in permeability may be caused by further narrowing of downstream fractures under the new stress of the high upstream pressure. There also exist several cross bedding fractures within the sample that may have been closed, decreasing permeability, due to the new stress applied from the increased inlet pressure.

Finally, while raising the downstream pressure of the sample, a recovery of the sample's initial permeability is seen. This shows that the decrease in permeability recorded for the increasing pressure drop across the sample was not caused by fines migration. The final recovered permeability in a stress state similar to that of the first recorded permeability is

expectedly lower, as some of the larger features holding the fracture open for fluid flow may have been compacted over the course of the tests.

The fracture void space from each tomogram was then segmented from the rest of the solid material. This segmentation was accomplished using a simple thresholding method instead of a more advanced watershed based algorithm, since the selection of appropriate phase label seeds within narrow near- or sub-resolution features proved to yield erroneous results due to an insufficient gradient between phases. Label seeds would also propagate inappropriately far into solid phase regions due to the lack of a significant greyscale gradient between suspected void space and solid. To assess the significance of the selected threshold value, three segmented images were created and used for flow simulations using a subjective optimal threshold value and deviations  $\pm 200$ .

This segmentation method was first applied to the dry scan images followed by the low confining pressure, and then high confining pressure system tomographies. As the stress applied to the system is increased, the aperture of the imaged fractures decreases and the accuracy of the segmentation of the fracture void became increasingly challenging as seen in **Figure 3**. Threshold segmentation was still found to yield the most representative of fracture segmentations, but the inclusion of numerous regions of noise within the solid regions of the sample significantly decreased the accuracy of the void space in each tomogram.

These erroneous regions were largely eliminated from the final fracture segmentation by computing the connected flow path along the flow direction of the sample using a neighbourhood selection allowing segmented voxels to be considered connected across edges, but not through vertexes. This analysis module then removes all disconnected components that are smaller than 10 voxels in a given volume. This greatly reduces the inclusion of non-connected, improperly segmented noise regions, but incorrect regions near the connected fracture space remain problematic. Previous work has attempted to tackle this issue of selecting a proper threshold value for features below image resolution [15] with the inclusion of looking at the connectivity factor or Euler-Poincaré number for 2D and 3D systems [16]. However, the distinction between erroneous regions attributed to the void space segmentation and simply void space regions below image resolution may have a significant effect and the analysis was not implemented here.

The high stress system proved to be beyond segmentation capabilities, as once a threshold segmentation value was found that had connectivity through the sample in the direction of flow, large errors were evident in the segmentation and excluded. A different greyscale value was selected for each tomography as the reconstruction bit scaling was different for each system based on how much overall resolvable fracture void space could be observed in the final reconstruction, as well as known x-ray source issues.

The segmented fracture void space data sets from the zero and low effective pressure conditions were processed using a Lattice-Boltzmann based flow simulation for the

determination of local velocity fields and single phase absolute permeability as shown in Error! Reference source not found.. The calculations were performed by mirroring the geometry about the flow face and using a constant uniform fluid body-force [17]. Experiment fluid flow and flow simulations were performed along the axial direction of the sample, the direction into the page for the shown images in **Figure 3**.

The preferential fluid flow path for the most conservative threshold image of the dry scan system can be seen in **Figure 5** following the results of the fluid flow simulation. The fluid flow path appears to be rather uniform throughout the fractured system flow network, with slight cross-bedding fluid exchange via smaller interlayer fractures. The two largest of fractures running through the sample appear to contribute the most to all fluid flow through the sample.

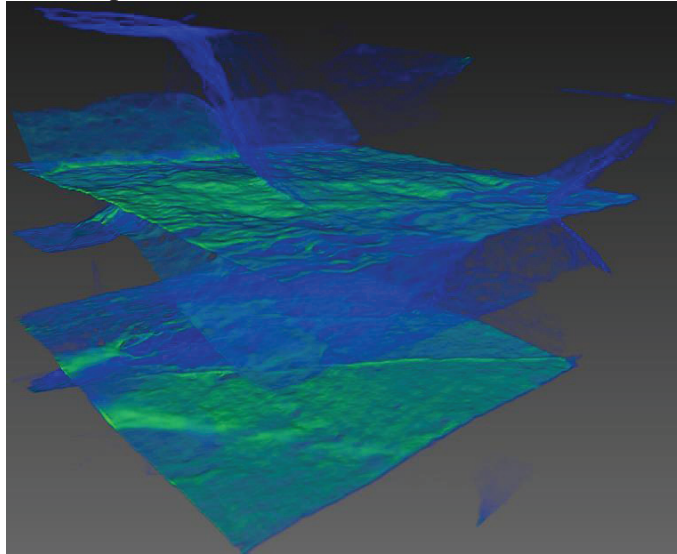


**Figure 5:** 3D representation of single phase fluid flow through segmented fracture system. Fluid flow occurred from the left front face to the rear right face of the extracted void space. Lighter colours represent areas of higher flow velocity with the darker blue being areas of lower velocity.

The two major lateral fractures running through the entire length of the observed region highlighted in **Figure 5** were extracted for analysis compared to the known solution for a system of two infinite parallel plates.

The flow rate between parallel plates is given by [18]:

$$\frac{Q}{l} = -\frac{\alpha^3 \Delta P}{12\mu L} \quad (1)$$

Where  $Q$  is the volumetric flow rate,  $l$  is the length normal to flow,  $\Delta P$  is the pressure difference across the length of the system,  $\alpha$  is the distance between the two plates,  $\mu$  is the fluid viscosity, and  $L$  is the length of the sample in the direction of flow. Then by

equating with Darcy's Law and solving for permeability, the following relation can be found:

$$k = -\frac{\alpha^3 l}{12A} \quad (2)$$

Where  $k$  is the sample permeability, and  $A$  being the sample area normal to flow. Predicted permeabilities for both the upper and lower major fractures as seen in the fluid flow representation are presented below in **Table 1** based on this calculation using the measured mean aperture from the original greyscale images. Crack apertures are a calculated mean value measured from greyscale images across 6 different orthogonal slices along the length of the sample.

**Table 1: Predicted permeability of fractured system using parallel plate model and Lattice-Boltzmann flow simulations compared to measured values. Note: The values presented for the flow simulation permeability calculations are based on the range of threshold values used for fracture segmentation.**

System		Crack Aperature (μm)	Crack Permeability (Darcy)	Combined Predicted Permeability (Darcy)	Flow Simulation Permeability (Darcy)	Measured Permeability (Darcy)
<b>Dry Scan</b>	Top Crack	101.5	10.16	14.7	15.3-44.6	N/A
	Bottom Crack	77.2	4.46			
<b>Low Stress</b>	Top Crack	23.8	0.14	0.71	0.63-2.52	0.001
	Bottom Crack	38.4	0.57			

These results show that the resulting permeabilities from the fluid flow simulations and those predicted by the parallel plate model correspond quite well. However, the predicted permeability at the low stress condition was much higher than that measured in the experiment. This was due to the fracture width being below the voxel size of the tomograms. To obtain a permeability of 1 mDarcy, the estimated aperture width of a planar fracture is 3.7 μm, well below the 13.2 μm voxel size of the scan. The fracture segmented from the scan has a width of at least one voxel, much too large to correctly represent the actual fracture system.

The effect of the matrix between fractures was assumed to be negligible, although fluid flow experiments on intact samples could not be completed as no unfractured plugs could be obtained. This assumption is supported by considering the orders of magnitude difference that exists between the imaged fracture apertures and the first major pore size peak appearing near 100 nm as seen in **Figure 1**. The lower values of measured permeability approaching the 1 μDarcy magnitude may be approaching that of the intact

matrix, and then would need to consider the effect of flow within the porous matrix structure.

A technique was then developed to measure qualitatively changes in overall fracture aperture along the length of the sample, making use of changes within the greyscale values for features below the resolvable limit. The mean greyscale value for the entire volume of interest ( $660 \times 635 \times 600 \mu\text{m}^3$ ) at each effective pressure was calculated and used to normalize the mean grey value for each slice in the plane orthogonal to flow along the length of the sample. Fluid flow occurs in direction of increasing slice number, or left to right in **Figure 6**. This analysis gives a qualitative analysis of sample void space for both above and below resolvable fracture features.

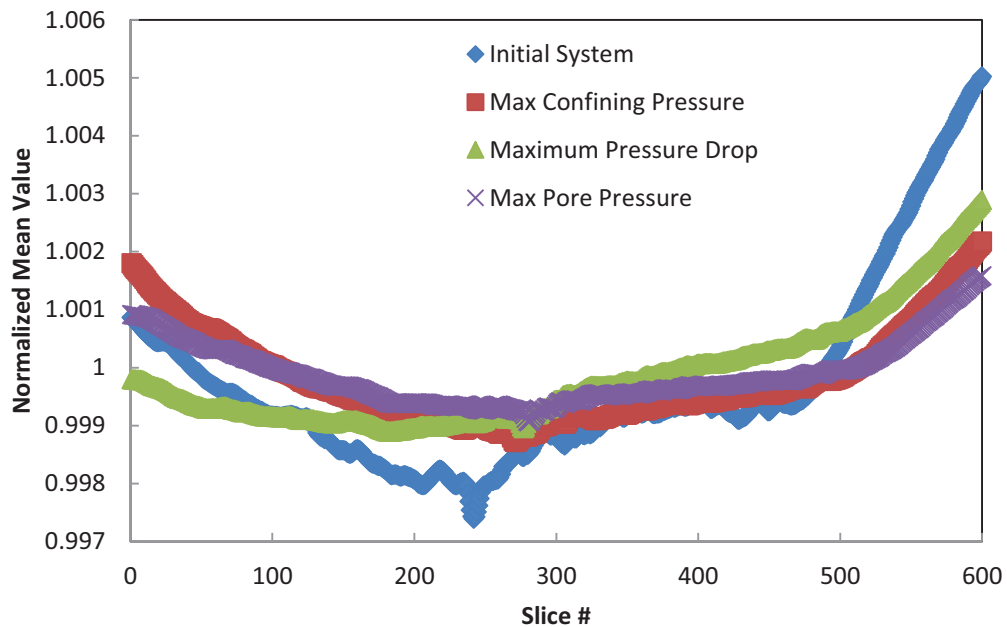


**Figure 6:** Normalized mean grey scale value of x-y plane orthogonal slices along length of sample for different stress systems.

The initial profile shows a high level of fluctuations with each advancing slice. These are caused by the large open and fully resolved fractures observed, which contribute a large portion of the potential fluid flow path. The profile at maximum confining pressure shows the homogenisation along with a smaller total spread of values caused by the closure of the fracture system. The maximum pressure drop data set shows the widening of upstream fractures with the slight dip seen in the left hand side of the figure compared to that of the maximum confining stress system, but with still a highly closed downstream portion. The final maximum pore pressure profile was similar to the maximum stress system, but has noticeably higher amounts of void space in the initial upstream and final downstream portions of the sample leading to the higher permeabilities. This final state also shows the unrecoverable change in system geometry following compaction by not returning to the level of fluctuations seen initially in the system.

The overall "U" shape of the final curves may be a result of beam hardening or lack of uniform x-ray delivery from the source cone shape leading to slight deviations from an overall mean value. This shape may also have been an effect of the compression in the axial direction of the sample caused by the unrestrained fluid inlets of the core-holder assembly, dissipating with depth into the fractured sample.

## CONCLUSIONS AND FUTURE WORK

The measurement of fractured system permeability under varying systems stresses was successfully recorded in a hassler type flow cell. Fractured sample permeability was found to decrease with increasing confining pressure under a constant, small pressure gradient. The near complete recovery of initial permeability was found to be possible by raising fluid pore pressure to the same initial effective pressure state. Full 3D x-ray micro-tomograms were collected after each change of system stress, and used to show qualitative changes in fracture void space. The fractured system was observed to exhibit no major change in permeability under a rising pressure gradient, despite evidence showing the widening of initial upstream fracture apertures. Upon raising pore pressure to reduce the effective pressure to close to the initial value, the sample recovered most of its initial permeability, with a slight decrease thought to be due to sample compaction. The limitations of system resolution for imaging the entire diameter of the sample limited the effectiveness of segmenting the fracture void space. The actual fracture aperture for even the lowest confining pressure was estimated to be well below the voxel size of the CT scan, and the image segmentation technique therefore overestimated the fracture width subsequently used in the Lattice-Boltzmann simulations.

## ACKNOWLEDGEMENTS

The authors would like to acknowledge the support of the Qatar Carbonates and Carbon Storage Research Centre (QCCSRC) for the funding of this project, as well as Shell, Qatar Petroleum, and Qatar Science and Technology Park for the funding of this program. The authors would also like to acknowledge fellow PhD candidate Farrel Gray for his contribution of the Lattice-Boltzmann fluid flow simulation results.

## REFERENCES

1. S. M. Benson and D. R. Cole, "CO<sub>2</sub> sequestration in deep sedimentary formations," *Elements*, vol. 4, pp. 325-331, 2008.
2. F. K. North, *Petroleum Geology*, 2nd ed. Winchester, Mass. 01890, USA: Allen & Unwin, 1985.
3. K. Edlmann, S. Haszeldine, and C. McDermott, "Experimental investigation into the sealing capability of naturally fractured shale caprocks to supercritical carbon dioxide flow," *Environmental earth sciences*, vol. 70, pp. 3393-3409, 2013.
4. A. Busch and A. Amann-Hildenbrand, "Predicting capillarity of mudrocks," *Marine and Petroleum Geology*, vol. 45, pp. 208-223, 2013.

- 5 A. Amann, M. Waschbüsch, P. Bertier, A. Busch, B. M. Krooss, and R. Littke, "Sealing rock characteristics under the influence of CO<sub>2</sub>," *Energy Procedia*, vol. 4, pp. 5170-5177, 2011.
- 6 A. Hildenbrand, S. Schrömer, and B. Krooss, "Gas breakthrough experiments on fine - grained sedimentary rocks," *Geofluids*, vol. 2, pp. 3-23, 2002.
- 7 P. Egermann, J. Lombard, and P. Bretonnier, "A fast and accurate method to measure threshold capillary pressure of caprocks under representative conditions," *SCA2006 A*, vol. 46, 2006.
- 8 N. J. Welch, J. P. Crawshaw, and E. S. Boek, "COMPARISON OF THE CHANGE OF CAP ROCK PERMEABILITY AND CAPILLARY ENTRY PRESSURE WITH VARYING EFFECTIVE STRESS," *SCA2014*, 2014.
- 9 S. Li, M. Dong, Z. Li, S. Huang, H. Qing, and E. Nickel, "Gas breakthrough pressure for hydrocarbon reservoir seal rocks: implications for the security of long - term CO<sub>2</sub> storage in the Weyburn field," *Geofluids*, vol. 5, pp. 326-334, 2005.
- 10 P. Boulin, P. Bretonnier, V. Vassil, A. Samouillet, M. Fleury, and J. Lombard, "Entry Pressure Measurements Using Three Unconventional Experimental Methods," presented at the International Symposium of the Society of Core Analysts, Austin, TX, USA, 2011.
- 11 A. RP40, "Recommended practices for core analysis," *Feb*, 1998.
- 12 M. Andrew, B. Bijeljic, and M. J. Blunt, "Pore-scale contact angle measurements at reservoir conditions using X-ray microtomography," *Advances in Water Resources*, vol. 68, pp. 24-31, 2014.
- 13 V. S. Group, "Avizo," 9.0 ed: FEI 2015.
- 14 A. Buades, B. Coll, and J.-M. Morel, "A non-local algorithm for image denoising," in *Computer Vision and Pattern Recognition, 2005. CVPR 2005. IEEE Computer Society Conference on*, 2005, pp. 60-65.
- 15 A. Samouëlian, H.-J. Vogel, and O. Ippisch, "Upscaling hydraulic conductivity based on the topology of the sub-scale structure," *Advances in water resources*, vol. 30, pp. 1179-1189, 2007.
- 16 H.-J. Vogel, "Topological characterization of porous media," in *Morphology of condensed matter*, ed: Springer, 2002, pp. 75-92.
- 17 S. M. K. Shah, J. P. Crawshaw, O. Gharbi, E. S. Boek, and J. Yang, "Predicting Porosity and Permeability of Carbonate Rocks From Core-Scale to Pore-Scale Using Medical CT Confocal Laser Scanning Microscopy and Micro CT," in *SPE Annual Technical Conference and Exhibition*, 2013.
- 18 R. W. Fox, A. T. McDonald, and P. J. Pritchard, *Introduction to Fluid Mechanics* 8th ed.: John Wiley & Sons, Inc., 2010.